nature materials

Article

https://doi.org/10.1038/s41563-024-02023-7

Obtaining $V_2(PO_4)_3$ by sodium extraction from single-phase $Na_xV_2(PO_4)_3$ ($1 < x < 3$) positive electrode materials

Received: 23 July 2023

Accepted: 12 September 2024

Published online: 23 October 2024

Check for updates

Sunkyu Park[1,2,3,11], Ziliang Wang[4,5,11], Kriti Choudhary[1], Jean-Noël Chotard[1,6], Dany Carlier[2,6], François Fauth[7], Pieremanuele Canepa[4,8,9] ✉, Laurence Croguennec[2,6] ✉ & Christian Masquelier[1,6,10] ✉

We report on single-phase $Na_xV_2(PO_4)_3$ compositions ($1.5 \leq x \leq 2.5$) of the Na super ionic conductor type, obtained from a straightforward synthesis route. Typically, chemically prepared c-$Na_2V_2(PO_4)_3$, obtained by annealing an equimolar mixture of $Na_3V_2(PO_4)_3$ and $NaV_2(PO_4)_3$, exhibits a specific sodium-ion distribution (occupancy of the Na(1) site of only 0.66(4)), whereas that of the electrochemically obtained e-$Na_2V_2(PO_4)_3$ (from $Na_3V_2(PO_4)_3$) is close to 1. Unlike conventional $Na_3V_2(PO_4)_3$, when used as positive electrode materials in Na-ion batteries, the $Na_xV_2(PO_4)_3$ compositions lead to unusual single-phase Na^+ extraction/insertion mechanisms with continuous voltage changes upon Na^+ extraction/insertion. We demonstrate that the average equilibrium operating voltage observed upon Na^+ deintercalation from single-phase $Na_2V_2(PO_4)_3$ is increased up to an average value of ~3.70 V versus Na^+/Na (thanks to the activation of the V^{4+}/V^{5+} redox couple) compared to 3.37 V versus Na^+/Na in conventional $Na_3V_2(PO_4)_3$, thus leading to an increase in the theoretical energy density from 396.3 Wh kg^{-1} to 458.1 Wh kg^{-1}. Electrochemical and chemical Na^+ deintercalation from c-$Na_2V_2(PO_4)_3$ enables complete Na-ion extraction, increasing energy density.

Lithium-ion batteries are widely used for electric vehicles and portable devices as they provide substantial energy and power densities, but lithium (Li) resources are critical and unevenly distributed worldwide, making it challenging to meet the urgent demand for large-scale energy storage systems[1,2]. Sodium-ion batteries have received much recent attention due to the more abundant and evenly distributed resources of sodium (Na)[3,4]. Sodium-containing transition metal layered oxides, Prussian blue analogues and polyanionic compounds are the main categories of positive electrode materials for Na batteries[5–8]. Phosphates having the Na super ionic conductor (NASICON) structure are potential options as positive electrode materials because of their structural stability, rate performance and long cycle life[5,9,10]. Among them, $Na_3V_2(PO_4)_3$ has been extensively studied, delivering a theoretical capacity of 117.6 mAh g^{-1} using the $V^{4+/3+}$ redox couple (3.37 V versus Na^+/Na), providing a theoretical energy density of ~396 Wh kg^{-1} (refs. 11–13). As a positive electrode material, two Na^+ ions can be reversibly exchanged through a biphasic mechanism between $Na_3V_2(PO_4)_3$ and $Na_1V_2(PO_4)_3$. However, the third Na^+ cannot be extracted because of the large migration energy of Na^+ from the Na(1) site and high redox potential[12,14], which contributes to a weight penalty in addition to moderate operating voltage.

Through simulated phase diagrams from density functional theory (DFT), cluster expansion and Monte Carlo calculations, as well as operando synchrotron X-ray diffraction (SXRD) during Na^+

A full list of affiliations appears at the end of the paper. ✉e-mail: pcanepa@central.uh.edu; laurence.croguennec@icmcb.cnrs.fr; Christian.masquelier@u-picardie.fr

https://doi.org/10.1038/s41563-024-02023-7

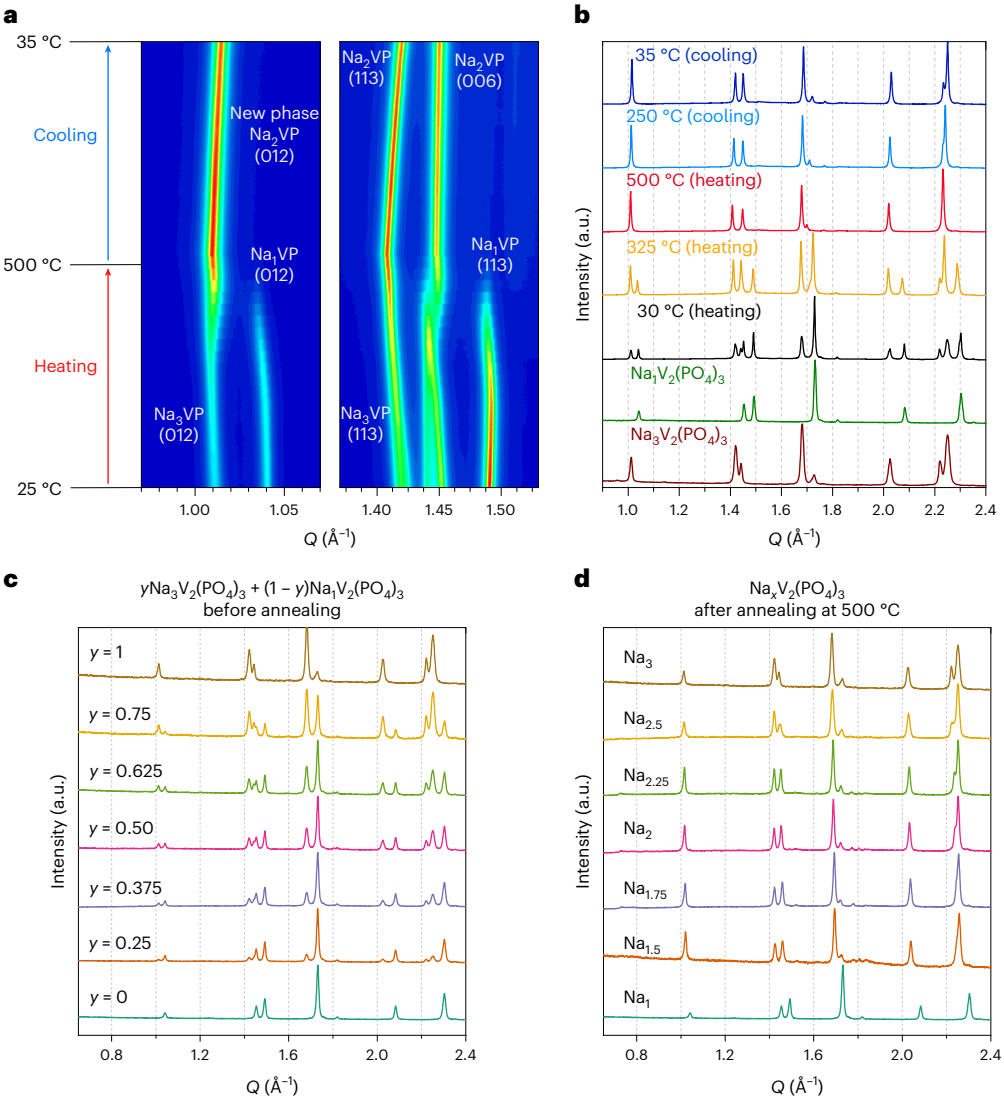

Fig. 1 | Synthesis of c-$Na_2V_2(PO_4)_3$. a, In situ temperature-controlled SXRD patterns for a 1:1 $Na_3V_2(PO_4)_3$/$Na_1V_2(PO_4)_3$ mixture, recorded every 3 °C upon heating up to 500 °C and then cooling to 35 °C. **b**, Comparison of key XRD patterns with those of pristine $Na_3V_2(PO_4)_3$ and $Na_1V_2(PO_4)_3$. **c**, XRD patterns of mixtures of $Na_3V_2(PO_4)_3$ and $Na_1V_2(PO_4)_3$ with different molar ratios before annealing, collected at 25 °C. **d**, XRD patterns of $Na_xV_2(PO_4)_3$ single phases after annealing, collected at 25 °C ($x = 2y + 1$). Note that $Na_xV_2(PO_4)_3$ is abbreviated as Na_xVP hereinafter. The complete series of XRD patterns collected with varying temperatures for different values of x are gathered in Supplementary Fig. 1a–e.

extraction/insertion, we have recently identified the existence of an intermediate $Na_2V_2(PO_4)_3$ phase between $Na_3V_2(PO_4)_3$ and $Na_1V_2(PO_4)_3$ (refs. 15,16). We determined the crystal structure of the electrochemically obtained e-$Na_2V_2(PO_4)_3$ and undertook substantial efforts to isolate this composition through various synthesis techniques. In this study we succeeded in chemically obtaining a new c-$Na_2V_2(PO_4)_3$ material that shows unusual and promising properties.

Spotting e-$Na_2V_2(PO_4)_3$ through electrochemistry

Extended Data Fig. 1 shows the SXRD patterns collected using a conventional $Na_3V_2(PO_4)_3$-containing electrode in an in situ half cell operating between 2.0 and 4.3 V versus Na metal at several charge–discharge rates. As observed in recent studies[15,17], an intermediate $Na_2V_2(PO_4)_3$ phase appears upon battery operation in between the phases of compositions $Na_3V_2(PO_4)_3$ and $Na_1V_2(PO_4)_3$. The intermediate, electrochemically obtained phase, (hereafter e-$Na_2V_2(PO_4)_3$) appears more visible at high cycling rates, with an intermediate unit-cell volume that allows mitigating volume changes, strains and a more pronounced phase separation[15], as identified in the $LiFePO_4$/$FePO_4$ system by the seminal work of Orikasa et al.[18].

Formation of c-$Na_xV_2(PO_4)_3$: temperature-controlled X-ray diffraction

As we discovered the existence of the e-$Na_2V_2(PO_4)_3$ phase during preliminary operando XRD measurements[15], we then naturally attempted to obtain the chemically prepared $Na_2V_2(PO_4)_3$ (hereafter c-$Na_2V_2(PO_4)_3$) through various synthesis procedures. We could apply a straightforward synthesis route to prepare single-phase c-$Na_xV_2(PO_4)_3$ compositions ($1.5 \le x \le 2.5$) by mixing the two end members $Na_3V_2(PO_4)_3$ and $Na_1V_2(PO_4)_3$ in appropriate ratios and annealing at moderate temperatures (500–550 °C). The pristine powders of both $Na_3V_2(PO_4)_3$ and $Na_1V_2(PO_4)_3$ were of high purity, and their unit-cell parameters were in excellent agreement with previously reported data[15,19]. Here we chose to use the hexagonal unit cell (space group R-3c) to describe the monoclinic structure of $Na_3V_2(PO_4)_3$ (refs. 15,19), for comparison purposes: lattice parameters $a = 8.7179(2)$ Å, $c = 21.8292(14)$ Å and $V/Z = 239.90(2)$ Å^3 where V/Z is the unit-cell volume per formula unit. $Na_1V_2(PO_4)_3$ was obtained as a single phase from $Na_3V_2(PO_4)_3$ by chemical oxidation, with the following lattice parameters: $a = 8.4276(2)$ Å, $c = 21.4731(4)$ Å and

https://doi.org/10.1038/s41563-024-02023-7

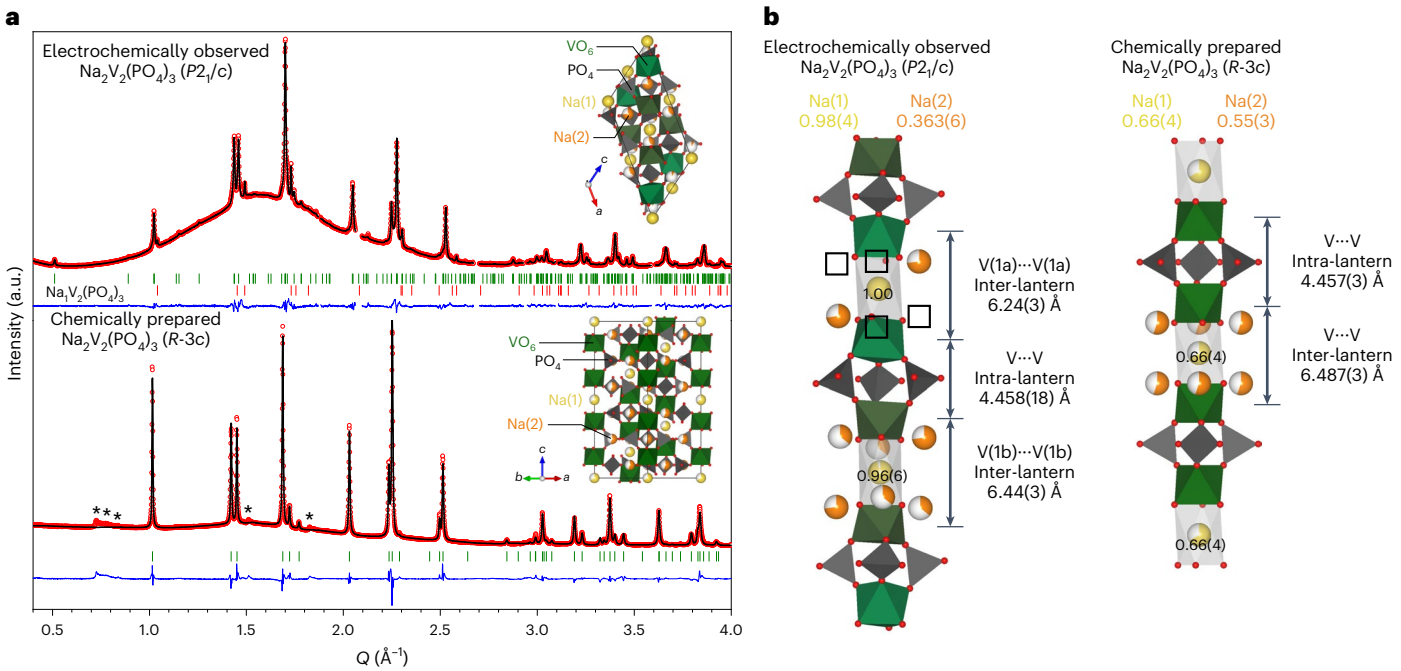

Fig. 2 | Structural variations in c-$Na_2V_2(PO_4)_3$ and e-$Na_2V_2(PO_4)_3$. a, SXRD patterns of $Na_2V_2(PO_4)_3$ at 25 °C. The top was collected with an in situ cell during electrochemical operation of a battery using a $Na_2V_2(PO_4)_3$ electrode as pristine material[15]. The bottom was chemically prepared c-$Na_2V_2(PO_4)_3$, collected within a capillary. The removed 2θ regions in the upper panel are ascribed to Al foil and Na metal. The asterisks in the bottom panel indicate reflection peaks that could not be indexed using the *R*-3*c* space group (details in the main text). The insets show the zoom out of $Na_2V_2(PO_4)_3$ crystal structures. In the SXRD patterns, red data points are observed data, black lines indicate the calculated XRD pattern, green and red vertical ticks indicate Bragg positions and blue lines are the difference between observed and calculated XRD patterns. **b**, Schematic representations of the $V_2(PO_4)_3$ lantern units with adjacent Na^+ ions in the crystal structures of electrochemically observed e-$Na_2V_2(PO_4)_3$ (left) and chemically prepared c-$Na_2V_2(PO_4)_3$ (right). We found two Wyckoff positions for vanadium in e-$Na_2V_2(PO_4)_3$ (e-Na_2VP), which are V(1a) and V(1b). Triple-dots correspond to the distance between V and V. Two V–V distances are represented: the distance between two vanadium sites belonging to the same lantern unit (intra-lantern) and the distance between two adjacent lantern units along the $[001]_{hex}$ direction (inter-lantern) of the hexagonal representation of the unit cell. Note that the e-Na_2VP displays two possible symmetries (space groups $P2_1/c$ or $P2/c$; ref. 15). We have demonstrated that $P2_1/c$ is a more suitable symmetry for the description of e-Na_2VP, which exhibits similar Na-vacancy populations with the theoretically predicted, ordered Na_2VP, considering that the temperature and the synthesis conditions can impact the e-Na_2VP structure at room temperature.

V/Z = 220.129(5) Å^3. This corresponds to a relative unit-cell volume reduction $\Delta V/V$ = −8.3% associated with the extraction of two Na^+ ions (and hence the oxidation of V^{3+} to V^{4+}) from $Na_3V^{3+}{}_2(PO_4)_3$, leading to $Na_1V^{4+}{}_2(PO_4)_3$.

Figure 1a,b illustrates the temperature-dependent transformation of a 1:1 $Na_3V_2(PO_4)_3/Na_1V_2(PO_4)_3$ mixture monitored by in situ SXRD. This leads to the formation of a single phase of composition $Na_2V_2(PO_4)_3$ at 500 °C, maintained as a single phase upon cooling to room temperature. During heating, the SXRD reflection peaks of the two pristine phases shift to lower 2θ angles due to thermal expansion (2θ, the angle between the incident beam and reflected beam). As the temperature was increased above ~300 °C, the two phases started merging concomitantly into c-$Na_2V_2(PO_4)_3$, and the reaction was fully completed at ~500 °C. During cooling, the SXRD reflection peaks of the c-$Na_2V_2(PO_4)_3$ single phase did not change, without phase separation down to 35 °C, with a slight continuous peak shift towards higher angles due to thermal contraction.

Noticeably, using the procedure described above (mixing and then annealing $y Na_3V_2(PO_4)_3 + (1-y)Na_1V_2(PO_4)_3$ powders at 500 °C), various target c-$Na_xV_2(PO_4)_3$ compositions (x = 1.5, 1.75, 2, 2.25, 2.5) were prepared. The corresponding SXRD patterns recorded at 25 °C (before and after annealing) are gathered in Fig. 1c,d. Before annealing, the pristine mixtures containing the two phases $Na_3V_2(PO_4)_3$ and $Na_1V_2(PO_4)_3$ can be clearly distinguished, with SXRD peak intensities being directly associated with the molar ratio of each phase (Fig. 1c). After annealing up to 500 °C, the two pristine mixtures of phases transformed into single phases of c-$Na_xV_2(PO_4)_3$ compositions (Fig. 1d). In c-$Na_xV_2(PO_4)_3$, all the main diffraction peaks can be indexed with the hexagonal cell and space group *R*-3*c*, with the peaks shifting towards lower 2θ angles for increasing values of x.

As determined by the Le Bail method and shown in Extended Data Fig. 2, the volume of the unit cell per formula unit (V/Z) decreases gradually when the Na content x varies from 2.5 to 1.5 in c-$Na_xV_2(PO_4)_3$, while the c/a ratio increases. Notably, the V/Z of the intermediate c-$Na_xV_2(PO_4)_3$ phases are found to be larger than those expected from the direct interpolation between the two end members, $Na_3V_2(PO_4)_3$ and $Na_1V_2(PO_4)_3$, probably nested in the partial occupancy of the Na(1) site in the chemically prepared c-$Na_xV_2(PO_4)_3$, while Na(1) is fully occupied in pristine $Na_3V_2(PO_4)_3$ and $Na_1V_2(PO_4)_3$. We report a single-phase composition with continuous unit-cell volume variation as a function of Na^+ content in $Na_xV_2(PO_4)_3$. Similarly, intermediate Li_xFePO_4 phases ($0 < x < 1$) discovered in 2005 by Delacourt et al.[20] were reported to form above 300 °C, prone to phase separation when cooled to room temperature (due to a eutectic point of $Li_{0.6}FePO_4$ encountered upon quenching)[20–25]. Likewise, similar foundational work on the $NaTi_2(PO_4)_3$–$Na_3Ti_2(PO_4)_3$ system was performed in the past through the formation of $Na_xTi_2(PO_4)_3$ single phases at ~900 °C, not stable at room temperature but disproportionate[26]. Delmas et al. also demonstrated the chemical short circuit method at the particle level by wetting a mixture of $Li_3Ti_2(PO_4)_3$ and $LiTi_2(PO_4)_3$ with an electrolyte to form an intermediate phase of composition $Li_{1.23}Ti_2(PO_4)_3$ (ref. 27). Here we discover that various intermediate single-phase c-$Na_xV_2(PO_4)_3$ compositions ($1.5 \le x \le 2.5$), stable at room temperature, can be accessed through an annealing process at moderate temperatures.

As mentioned earlier[15,16], an original phase of e-$Na_2V_2(PO_4)_3$ composition had been electrochemically observed during battery operation, and its crystal structure differs substantially from that of the

https://doi.org/10.1038/s41563-024-02023-7

Table 1 | Computed volumes, relative energies (relative to e-GS), occupation of the Na(1) and Na(2) sites and V–V distances for $Na_1V_2(PO_4)_3$, $Na_{1.5}V_2(PO_4)_3$ and $Na_2V_2(PO_4)_3$

$Na_xV_2(PO_4)_3$	State	Volume ($Å^3$f.u.$^{-1}$)	Δ*E* (meV per atom)	Na(1)-occ	Na(2)-occ	*d*(V–V) (Å)	*D*(V–V) (Å)
***x*=1**	e-GS	219.499	0	1.00	0	4.543	6.042
	Metastable-α	220.063	10.56	0.75	0.08	4.554	6.083
	Metastable-β	221.168	21.06	0.50	0.17	4.549	6.142
	Metastable-γ	222.716	26.44	0.25	0.25	4.559	6.145
***x*=1.5**	e-GS	223.465	0	1.00	0.17	4.531	6.088
	Metastable-α	224.648	5.68	0.75	0.25	4.529	6.166
	Metastable-β	225.000	12.43	0.50	0.33	4.512	6.196
***x*=2**	e-GS	227.159	0	1.00	0.33	4.510	6.156
	Metastable-α	228.870	6.00	0.75	0.42	4.547	6.196
	Metastable-β	230.242	10.26	0.50	0.50	4.525	6.294

Metastable refers to the structure with a partially occupied Na(1) site and has the lowest relative energy Δ*E* among its analogues with the same Na(1)-occ; Na(1)-occ, occupation of Na(1) site; Na(2)-occ, occupation of Na(2) site. Different metastable configurations, as characterized by their unique Na(1) or Na(2) occupation, are indicated as α, β and γ. The *d*(V–V) is the average distance between two vanadium sites belonging to the same lantern unit; *D*(V–V) corresponds to the average V–V distance between two adjacent lantern units along the $[001]_{hex}$ direction. Computed density of states for different phases and a schematic of the structural distribution of Na and vacancies are given in the Supplementary Information. Reminder, Na(1)+3Na(2)=*x* in $Na_xV_2(PO_4)_3$.

c-$Na_2V_2(PO_4)_3$ obtained by the chemical reaction of the mixture of the two end members, as discussed now. Figure 2a compares the corresponding SXRD patterns, indexed in the $P2_1/c$ and $R\text{-}3c$ space groups, respectively. The reflection peaks observed at Q (with $Q = 4\pi \cdot \sin(\theta)/\lambda$ and λ the wavelength of the X-ray radiation) = 0.51, 1.15 and 1.25 $Å^{-1}$ for the e-$Na_2V_2(PO_4)_3$ phase (indexed with a monoclinic cell, $P2_1/c$) are absent in the c-$Na_2V_2(PO_4)_3$ phase in the rhombohedral space group $R\text{-}3c$. For the c-$Na_2V_2(PO_4)_3$ phase, some diffraction peaks are unindexed (marked with asterisks). Using several commonly observed space groups for NASICON compositions, such as $R32$, $P2/m$, $P2/c$, $P2_1/c$ and $P\text{-}1$, the monoclinic space group $P2/m$ with lattice parameters a = 14.8094 Å, b = 8.6597 Å, c = 7.4997 Å, the angle β = 99.7135° and V/Z = 237.00 $Å^3$ could fully index the experimental XRD pattern of c-$Na_2V_2(PO_4)_3$ (Extended Data Fig. 3). However, some of these diffraction peaks at 0.65–0.9 $Å^{-1}$ in Q space are asymmetric and 'diffuse', which prevented us from finding a full description of the structure. Therefore, an average structure of higher symmetry ($R\text{-}3c$) was used in this study to describe c-$Na_2V_2(PO_4)_3$, as this approach had been shown[15] to be highly appropriate for describing the Na distribution in e-$Na_2V_2(PO_4)_3$. Indeed, in both descriptions of e-$Na_2V_2(PO_4)_3$ (using the average ($R\text{-}3c$) or more precise ($P2_1/c$) structures), the Na(1) sites (labelled Na(1) in $R\text{-}3c$ and Na(1a), Na(1b) in $P2_1/c$) are always fully occupied[15], the monoclinic distortion being nested in the Na(2) ordering. As shown in Extended Data Fig. 4 in the average structure ($R\text{-}3c$), some diffraction peak intensities in the simulated XRD patterns are strongly influenced by the respective Na(1) and Na(2) site occupancies, in particular at Q = 1.015 $Å^{-1}$ (that is, $(012)_{R\text{-}3c}$). We find that the Na(1) = 0.66(4) and Na(2) = 0.55(3) distribution is the most adequate.

The cell parameters, the sodium occupancy factors and the V–O distances of both e-$Na_2V_2(PO_4)_3$ and c-$Na_2V_2(PO_4)_3$ were analysed by Rietveld refinements, as summarized in Extended Data Table 1. It appears that both e-$Na_2V_2(PO_4)_3$ and c-$Na_2V_2(PO_4)_3$ are similar in that they have the same NASICON-type framework, but a substantial difference exists in the distribution of sodium ions between the two compounds. In the case of e-$Na_2V_2(PO_4)_3$, the Na(1) site is fully occupied, and one-third of the Na(2) site is filled. Both structural models ($P2_1/c$ and $R\text{-}3c$) for e-$Na_2V_2(PO_4)_3$ show excellent correlation between cell volumes, sodium occupancies and V–O distances. By contrast, in the case of c-$Na_2V_2(PO_4)_3$, Na(1) is not fully occupied but two-thirds occupied, and the remaining Na^+ ions are located at the Na(2) site (0.55(3)). This can be supported by examining the V–V distances in the NASICON structure. On the one hand, both structures (e-$Na_2V_2(PO_4)_3$ and c-$Na_2V_2(PO_4)_3$) have a similar V–V distance within a given lantern unit (intra-lantern), with values of 4.458(18) Å and 4.457(3) Å, respectively. On the other hand, the V–V distances along the $[001]_{hex}$ direction between two different lantern units (inter-lantern) are different for e-$Na_2V_2(PO_4)_3$ and c-$Na_2V_2(PO_4)_3$. In e-$Na_2V_2(PO_4)_3$, the inter-lantern V–V distance is 6.24(3) Å, whereas in c-$Na_2V_2(PO_4)_3$, it is 6.44(3) Å. These important differences suggest that the structures are noticeably different. Indeed, since the Na(1) sites are located between two lantern units along $[001]_{hex}$, partial occupation implies lower screening (that is, stronger electrostatic repulsions) between triangular oxygen octahedral faces from two lantern units, and thus longer inter-lantern V–V distances. Note that an empty or partially filled Na(1) site in the NASICON structure is very rarely encountered. Na-free NASICON structures include $Fe^{III}_2(SO_4)_3$, $NbTi(PO_4)_3$ and $Nb_2(PO_4)_3$ (ref. 5). The Na(1) site is fully occupied in $NaTi_2(PO_4)_3$ (ref. 28), $Na_3Fe_2(PO_4)_3$ (ref. 29), $Na_2TiFe(PO_4)_3$ (ref. 30), $Na_2TiCr(PO_4)_3$ (ref. 31) and $Na_2VTi(PO_4)_3$ (refs. 32,33). Hence, the partial occupancy of the Na(1) site in c-$Na_2V_2(PO_4)_3$ appears rather unique, which we attempt to rationalize.

The relatively high temperature (~500 °C) we used for preparing c-$Na_3V_2(PO_4)_3$ is probably the origin of the main difference in Na(1) site occupancy when compared with e-$Na_3V_2(PO_4)_3$, obtained at room temperature through a solid–liquid interface. We previously demonstrated that in $Na_3V_2(PO_4)_3$, the population of the Na(1) site changes with temperature, from fully occupied in the α-monoclinic phase ($C2/c$) at room temperature to fractional occupancies in the γ-rhombohedral phase ($R\text{-}3c$) at 200 °C (ref. 19). Therefore it is possible that the reaction of $Na_3V_2(PO_4)_3$ with $Na_1V_2(PO_4)_3$ at ~500 °C may produce c-$Na_xV_2(PO_4)_3$ with fractional occupancies at the Na(1) site.

These experimental findings and interpretations are further strengthened by our published theoretical work[16] that highlights the presence of a single-phase region associated with the mixed-valence phase $Na_2V_2(PO_4)_3$, as illustrated in Supplementary Fig. 5. At 300 K, no isolated single phase would be expected while performing electrochemistry between $Na_3V_2(PO_4)_3$ and $Na_1V_2(PO_4)_3$, and thus e-$Na_2V_2(PO_4)_3$ obtained from an operando electrochemical experiment performed at room temperature should be mixed with the $Na_1V_2(PO_4)_3$ phase or the $Na_3V_2(PO_4)_3$ phase. However, when higher temperature syntheses are conducted, that is, at temperature T > 500 K, the stability region of $Na_2V_2(PO_4)_3$ is much enlarged, and thus c-$Na_2V_2(PO_4)_3$ tends to exist as an isolated thermodynamic single phase. Our theoretical works[16,34] have confirmed the possibility of probing disordered $Na_1V_2(PO_4)_3$, $Na_{1.5}V_2(PO_4)_3$ and $Na_2V_2(PO_4)_3$ configurations, characterized by the specific partial fractional occupations of both Na(1) and Na(2) sites, thus explaining the chemically prepared or electrochemically obtained phases. We found

https://doi.org/10.1038/s41563-024-02023-7

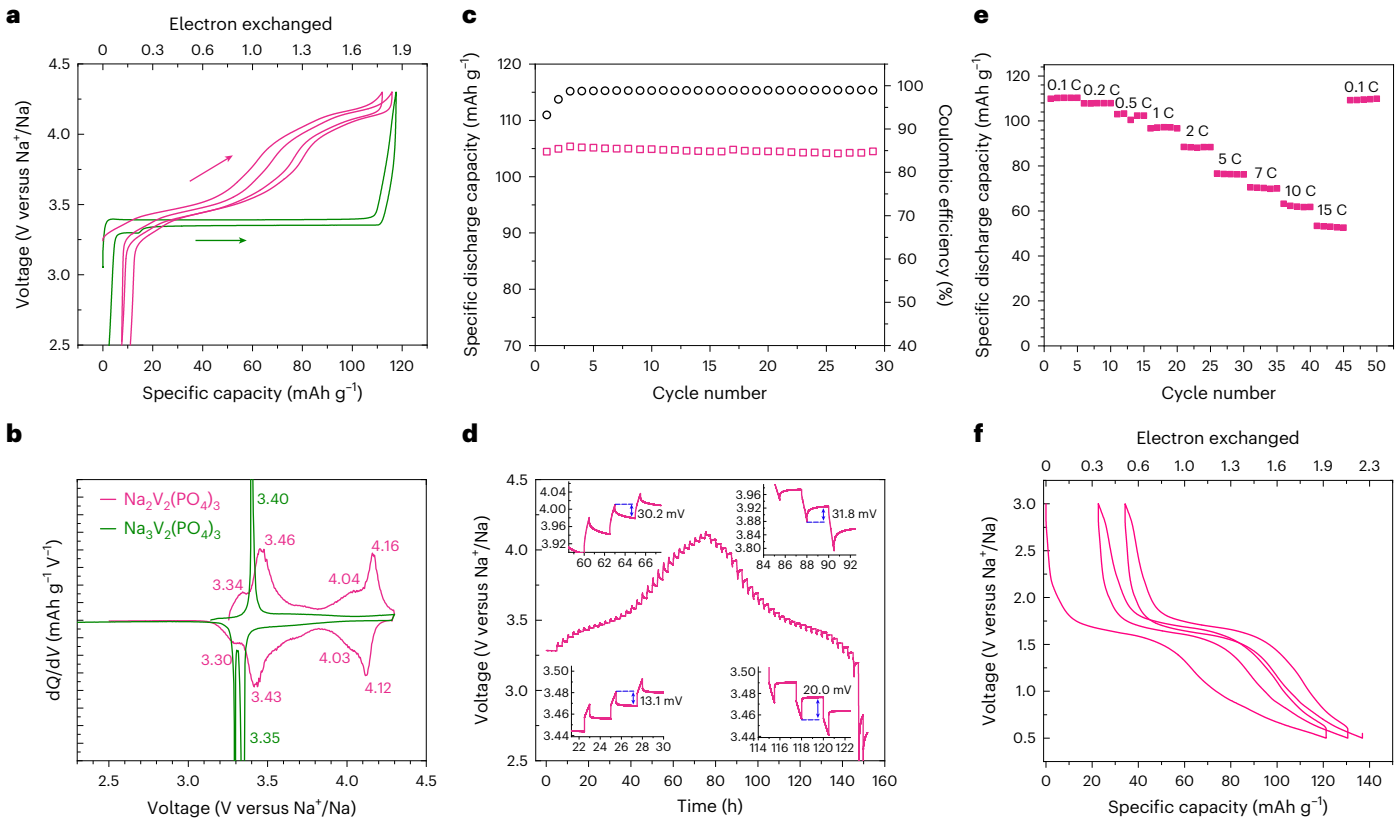

Fig. 3 | Electrochemistry of c-$Na_2V_2(PO_4)_3$. **a**, Electrochemical charge and discharge profiles of $Na_2V_2(PO_4)_3$ (green) and c-$Na_2V_2(PO_4)_3$ (pink) electrodes cycled between 2.5 and 4.3 V at C/10 (one Na^+ in 10 h) versus Na metal. **b**, Derivative (d*Q*/d*V*) plots of the first charge and discharge cycles obtained for c-$Na_2V_2(PO_4)_3$ and $Na_3V_2(PO_4)_3$ electrodes. **c**, Discharge capacities and coulombic efficiencies of the c-$Na_2V_2(PO_4)_3$ electrode upon 30 cycles. **d**, GITT curve of c-$Na_2V_2(PO_4)_3$ electrode versus Na metal during the first electrochemical charge–discharge cycle. The insets show zoomed-in views. **e**, Rate capability of c-$Na_2V_2(PO_4)_3$ electrode versus Na metal with various C rates from 0.1 C to 15 C. **f**, Electrochemical charge and discharge profiles of c-$Na_2V_2(PO_4)_3$ electrodes cycled between 1.3 and 3.0 V at C/10.

that the local charge arrangements on the vanadium sites with higher/lower oxidation states may disrupt potentially stable structural arrangement between Na ions and their vacancies in $Na_1M_2(PO_4)_3$, thus lowering the migration barriers and enhancing the jump diffusivity of Na^+, which, in turn, will enable the extraction of the 'last' Na^+ ion. For example, some of us recently determined that if compositions with low Na content (that is, $Na_{0+x}V_2(PO_4)_3$ with $x < 1$) were thermodynamically stable, the Na^+ extraction from $Na_1V_2(PO_4)_3$ towards an empty Na phase (that is, $V_2(PO_4)_3$) would be kinetically facilitated by the local charge arrangement of the mixed-valence vanadium sites $V^{4+/5+}$ at highly charged state[34].

To complement these statements, Table 1 provides energetics computed with first-principles calculations of different Na-vacancy orderings, whose Na site occupations correspond to the c-$Na_2V_2(PO_4)_3$ and e-$Na_2V_2(PO_4)_3$ structures. These calculations rationalize the structural differences between the c-$Na_2V_2(PO_4)_3$ and e-$Na_2V_2(PO_4)_3$ structures. The electrochemically observed $Na_2V_2(PO_4)_3$ phase is the ground state (electrochemical ground state, e-GS in Table 1), whereas the chemically prepared c-$Na_2V_2(PO_4)_3$ phase appears as a metastable structure. Indeed, the first is characterized by the full occupancy of the Na(1) site, whereas the second shows fractional occupations of the Na(1) and Na(2) sites. Table 1 also shows the computed Na-disordered structures for $Na_{1.5}V_2(PO_4)_3$ and $Na_1V_2(PO_4)_3$ compositions (Supplementary Figs. 6 and 7). The e-GS shows full occupation of the Na(1) site, whereas the metastable structures (α/β/γ) display a partially occupied Na(1) site. Note that for an equal Na distribution among the Na(1) and Na(2) sites, $Na_2V_2(PO_4)_3$, $Na_{1.5}V_2(PO_4)_3$ and $Na_1V_2(PO_4)_3$ show very mild metastability (with energies of <25 meV per atom). This indicates that changes in Na-vacancy orderings (to accommodate changes in the composition) in the metastable structures (α/β/γ) can be accessed electrochemically, which is a strong indication of the solid solution mechanism for Na^+ extraction from these compositions. The depopulation of the Na(1) site in the metastable structures increases the volume (per formula unit) in $Na_xV_2(PO_4)_3$ versus the corresponding e-GS (Table 1 and Supplementary Fig. 8), in excellent agreement with volumes experimentally determined from Rietveld refinements for c-$Na_xV_2(PO_4)_3$ and e-$Na_xV_2(PO_4)_3$ (Extended Data Table 1). Notably, a $Na_2V_2(PO_4)_3$ configuration that has similar Na(1) and Na(2) occupations (that is, 0.66 for Na(1) and 0.55 for Na(2), for an effective composition of $Na_{2.31(12)}V_2(PO_4)_3$) exhibits a larger cell volume by ~1.4% than the corresponding ordered e-GS structure (that is, e-$Na_2V_2(PO_4)_3$). As mentioned earlier, this increase of the unit-cell volume in $Na_2V_2(PO_4)_3$ can be attributed to a depopulation of the Na(1) sites that increases the inter-lantern vanadium–vanadium distance (*D*(V–V); Fig. 2b). Hence we show that the partial occupation of the Na(1) site induces an increase in the unit-cell volume per formula unit, but with small changes in energies (<25 meV per atom), moving from the ordered to the disordered structures. In all three compositions examined, that is, $x = 1$, $x = 1.5$ and $x = 2.0$, the metastability of Na-vacancy orderings in $Na_xV_2(PO_4)_3$ appears accessible at room temperature, which indicates that these c-$Na_xV_2(PO_4)_3$ phases are accessible via electrochemical methods due to high Na solubility in this NASICON framework.

Electrochemical properties of c-$Na_2V_2(PO_4)_3$

The electrochemical properties of c-$Na_2V_2(PO_4)_3$ were investigated and are compared with those obtained for the conventional well-known $Na_3V_2(PO_4)_3$ (Fig. 3). Charge and discharge voltage–composition

https://doi.org/10.1038/s41563-024-02023-7

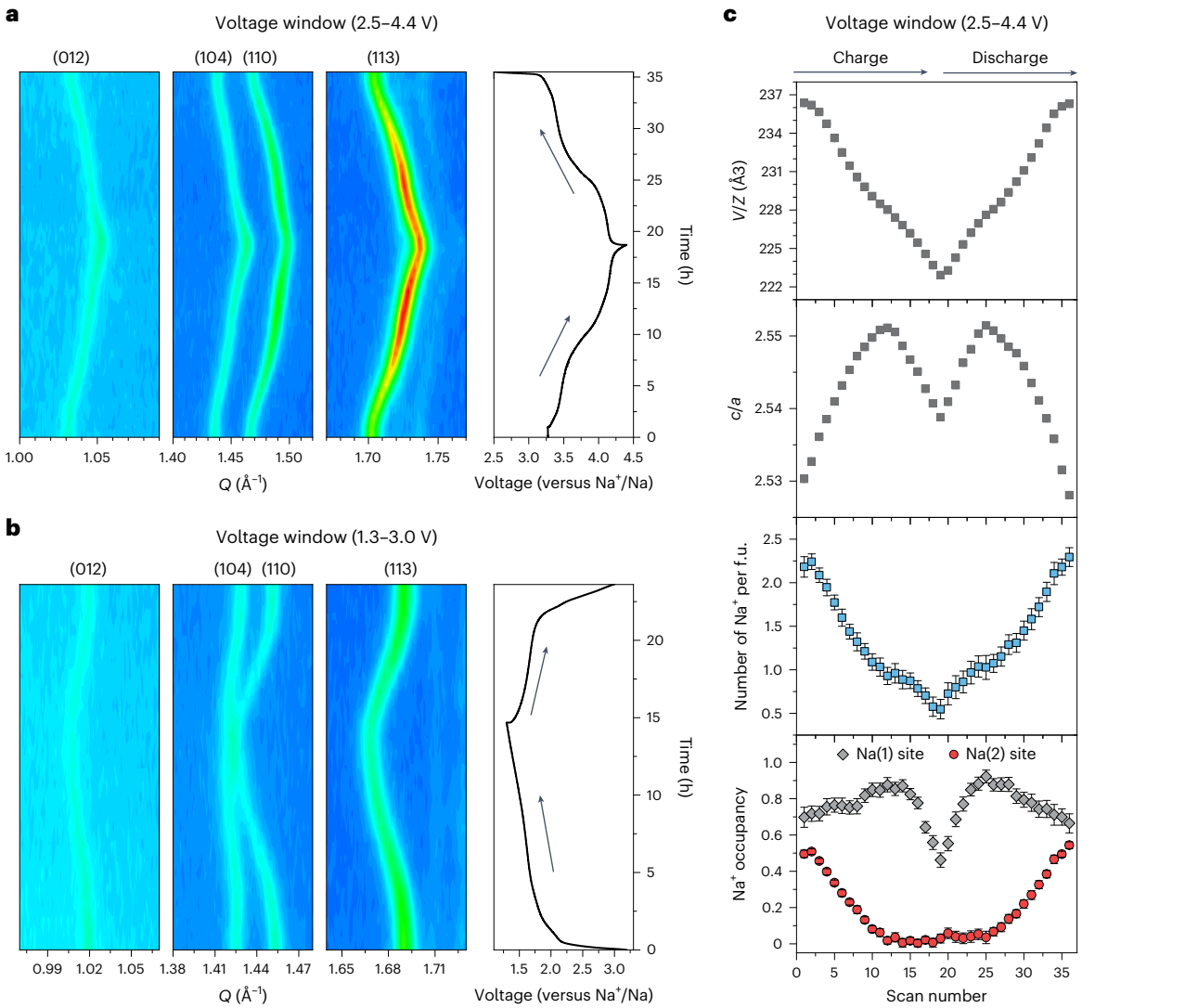

Fig. 4 | Structural evolution during battery operation. a,**b**, Operando XRD measurements using c-$Na_2V_2(PO_4)_3$ as a positive electrode in a half cell versus Na metal upon charge and discharge cycles, within voltage windows of 1.3–3.0 V (**b**) versus Na^+/Na at C/10 (that is, one Na^+ in 10 h) and 2.5–4.4 Volts (**a**). The right-hand plot shows voltage over time. **c**, Corresponding results (Na site occupancies, number of Na^+ per formula unit (f.u.), *c*/*a* ratio and *V*/*Z*) from Rietveld refinements within the voltage window of 2.5–4.4 Volts upon charge (scan numbers 1–19) and discharge (scan numbers 19–36). The error bars refer to standard deviations arising from the Rietveld refinements.

profiles of $Na_2V_2(PO_4)_3$ obtained during the first two cycles, with a half-cell configuration versus Na metal, are represented in Fig. 3a. Remarkably, c-$Na_2V_2(PO_4)_3$ (in pink) exhibits a sloping voltage–composition profile, unlike conventional $Na_3V_2(PO_4)_3$ (in green), which operates through a voltage–composition plateau at around 3.37 Volts versus Na. The first charge and discharge capacities of c-$Na_2V_2(PO_4)_3$ are 112 and 104 mAh g^{-1}, respectively.

Approximately 1.8 Na^+ per formula unit was extracted from c-$Na_2V_2(PO_4)_3$ during the first charge, meaning that much less than one Na^+ remains in the structure at the end of charge. This fact is remarkable, as for many other vanadium (V)-based NASICON-type materials, including the conventional $Na_3V_2(PO_4)_3$, one Na^+ ion (that is, $Na_1V_2(PO_4)_3$) always remains in the structure at the end of the charge[35–40]. In addition, $Na_2V_2(PO_4)_3$ operates at a much increased average voltage of ~3.70 Volts versus Na, compared to 3.37 Volts for the conventional $Na_3V_2(PO_4)_3$. As evidenced by the differential capacity curve (d*Q*/d*V* versus *V*) of Fig. 3b, the voltage–composition profile observed upon Na^+ extraction from c-$Na_2V_2(PO_4)_3$ can be divided into two domains, at around 3.42 and 4.12 V versus Na, respectively. Approximately two Na^+ ions are reversibly extracted from $Na_2V^{3+}V^{4+}(PO_4)_3$, and the two distinct domains are ascribed to (1) the $V^{4+/3+}$ redox couple at ~3.45 V versus Na/Na^+ and (2) the $V^{5+/4+}$ redox couple at ~4.15 V versus Na/Na^+. Indeed, prior work on $Na_xMV(PO_4)_3$ (M = Al (ref. 37), Mn (refs. 41–49) or Fe (refs. 50–53)) by us and others has identified the $V^{5+/4+}$ redox couple in NASICONs at a voltage close to ~4.0 Volts. Importantly, the redox activity at ~4.10 Volts of c-$Na_2V_2(PO_4)_3$ signifies that such electrodes possess a theoretical energy density approximately 15.5% higher than conventional $Na_3V_2(PO_4)_3$, exhibiting a discharge capacity of 104 mAh g^{-1} after 29 cycles (Fig. 3c). In addition, galvanostatic intermittent titration technique (GITT) experiments of c-$Na_2V_2(PO_4)_3$ recorded during the first electrochemical cycle show a small overpotential (around 10–30 mVolts) over the whole voltage range during both charge and discharge, indicating good kinetics for Na^+ diffusion (Fig. 3d). This is further shown in Fig. 3e, which illustrates the rate capability of the studied material measured for several rates expressed in units of C from 0.1 C to 15 C, with a 1 C rate meaning full charge over a period of 1 h (and 0.1 C a full charge over 10 h and 15 C a full charge in 4 min). The discharge capacity measured at 15 C corresponds to 48.6% of that obtained at 0.1 C.

As shown in Fig. 3f, approximately two Na^+ ions can be reversibly intercalated into c-$Na_2V_2(PO_4)_3$, down to 0.5 Volts versus Na^+/Na, most likely including partial electrolyte degradation through a parasitic reaction at low voltage (solid electrolyte interphase (SEI)). Extended Data Fig. 5 further supports this as it illustrates the full reversibility of the overall system, between 0.5 and 4.5 Volts for a global utilization of the $Na_xV_2(PO_4)_3$ framework with $0 \le x \le 4$. This may open the door for fabricating symmetrical $Na_2V_2(PO_4)_3$/electrolyte/$Na_2V_2(PO_4)_3$ cells, with liquid or solid electrolytes.

Using the local cluster expansion-based model of Wang et al.[34], we further evaluated the migration barriers of Na^+ for different phases of $Na_2V_2(PO_4)_3$, that is, the e-GS with fully occupied Na(1); metastable α-state with Na(1) occupancy of 0.75; and metastable β-state with Na(1) occupancy of 0.5 (Table 1). Na^+ migration barriers between the Na(1) and Na(2) sites in $Na_2V_2(PO_4)_3$ tend to decrease, following the sequence of ~744.9 meV for e-GS > ~602.3 meV for metastable α-state > ~438.0 meV for metastable β-state structures. This decrease of Na^+ migration barriers in $Na_2V_2(PO_4)_3$ configurations with less-occupied Na(1) sites indicates that disorder among the Na(1) and Na(2) sites eases the kinetics of Na^+ migration through vacancy-mediated mechanisms.

Structural evolution upon Na^+ extraction/insertion

To investigate the structural evolution and Na^+ extraction/insertion mechanism of $Na_2V_2(PO_4)_3$, operando SXRD experiments were performed, between 1.0 and 4.4 Volts versus Na^+/Na at a C rate of C/9 (one Na^+ is extracted in ~9 h), as illustrated in Fig. 4. The single-phase reaction mechanism inferred from the sloping voltage–composition profile is confirmed. The XRD reflection peaks continuously shift, reversibly, towards higher or lower *Q* space during charge or discharge (Fig. 4a,b), and accordingly the unit-cell volume gradually decreases or increases (Fig. 4c). While 'classical' $Na_3V_2(PO_4)_3$ has a flat voltage–composition profile with two successive two-phase reactions ($Na_3V_2(PO_4)_3$–$Na_2V_2(PO_4)_3$ and $Na_2V_2(PO_4)_3$–$Na_1V_2(PO_4)_3$), c-$Na_2V_2(PO_4)_3$ shows an entirely different reaction mechanism for Na^+ extraction: a sloping voltage–composition profile and a full solid solution mechanism over the explored voltage region. We propose that the different reaction mechanisms are nested in the different occupation factors of the Na(1) site in e-$Na_2V_2(PO_4)_3$ and c-$Na_2V_2(PO_4)_3$. When V-based NASICON compounds, such as $Na_4MnV(PO_4)_3$ and $Na_4FeV(PO_4)_3$, involve V^{4+}/V^{5+} vanadium redox reactions at high voltage, above 3.9 Volts versus Na^+/Na, they often experience an asymmetric electrochemical reaction mechanism in the following discharge[35–53]. Interestingly, this is not the case for the chemically prepared c-$Na_2V_2(PO_4)_3$. The overall electrochemical reaction is highly reversible and favours electrochemical operation over an extensive number of cycles.

The quantitative structural analysis through Rietveld refinements of the operando SXRD data also shows that the electrochemical reaction during charge and discharge is highly symmetric and reversible (Fig. 4 and Extended Data Table 2). Upon charging to 3.8 Volts versus Na, one Na^+ can be extracted and as a consequence, one Na^+ still remains in the structure, with partially occupied Na(1) and Na(2) sites. The refined parameters of $Na_1V_2(PO_4)_3$ obtained from c-$Na_2V_2(PO_4)_3$ are summarized as they are highly sensitive to the sodium content on the Na(1) site. Interestingly, while having the same composition, 'classical' $Na_1V_2(PO_4)_3$ obtained from the extraction of two Na^+ ions from $Na_3V_2(PO_4)_3$ shows different unit-cell dimensions (a = 8.4276(2) Å, c = 21.4731(4) Å, V/Z = 220.13(1) Å^3) with Na(1) fully occupied and empty Na(2) sites. The V/Z volumes of the pristine material and of that recovered at the end of charge are 236.35(2) Å^3 and 222.92(2) Å^3, respectively, which means that the overall volume change is less than 6% (5.7%; Extended Data Table 2). This is lower than the volume change between 'conventional' $Na_3V_2(PO_4)_3$ and $Na_1V_2(PO_4)_3$ (about 8.2%). Interestingly, the c/a ratio increases up to around mid-charge (scan no. 12) and then decreases until the end of charge. When it comes to Na^+ occupancy, the total number of Na^+ ions in the structure gradually decreases during charge and then increases during discharge. However, the contribution to the decreasing number of Na^+ ions until mid-charge is due to the depopulation of the Na(2) site with a partial transfer of Na^+ ions from the Na(2) site to the Na(1) site: the decreasing occupancy of Na(2), until zero at mid-charge, is thus observed in parallel with an increasing occupancy of Na(1). From scan no. 14, the depopulation of the Na(1) site occurs until the end of charge (Fig. 4c).

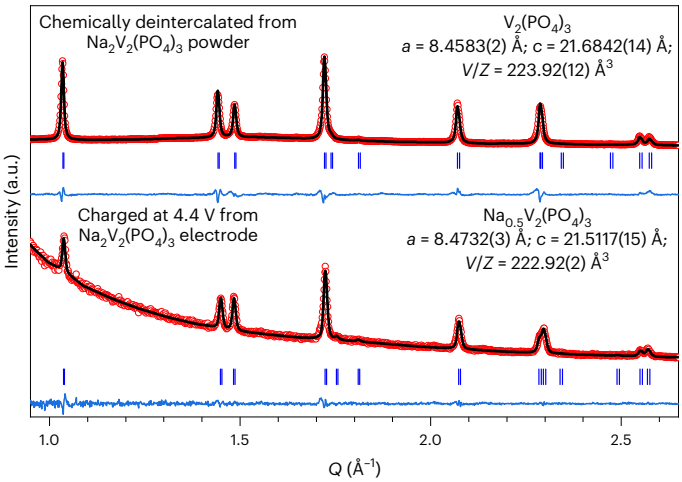

Fig. 5 | XRD patterns of $Na_xV_2(PO_4)_3$ (x close to 0). Rietveld refinements of the XRD patterns collected at the end of charge (4.4 V) during operando measurement and for the chemically deintercalated phase from the c-$Na_2V_2(PO_4)_3$ powder. Refined structural parameters are listed in Extended Data Table 3.

To ensure full oxidation of c-$Na_2V_2(PO_4)_3$, and for comparison to the composition obtained operando at the end of charge, chemical deintercalation from c-$Na_2V_2(PO_4)_3$ was carried out. The XRD profiles analysed by Rietveld refinements and structural parameters are compared in Fig. 5. The a parameter is further decreased for the chemically deintercalated phase in comparison to that observed for the composition recovered at the end of charge. By contrast, the c and V/Z parameters slightly increase. The occupancy factors for the Na(1) and Na(2) sites after the chemical deintercalation are zero, suggesting that full extraction of Na was achieved after the chemical oxidation process. The value of the V–O distance also supports this: it was 1.89(15) Å after chemical deintercalation but 1.92(3) Å at the end of the charge of up to 4.4 V versus Na^+/Na. We were able to obtain the composition $V_2(PO_4)_3$ with no residual alkali ions in the NASICON host structure and with a smaller V/Z unit-cell volume reported for a $Na_xV_2(PO_4)_3$ NASICON structure (Extended Data Table 3).

This study presents a different class of NASICON-related materials synthesized by a straightforward route. The great tunability of NASICON materials will allow many transition metals to be substituted, and thus we envisage many different NASICON-type compositions being discovered, containing Ti, V, Fe or Mn as redox-active transition metal elements. The unconventional synthesis procedure developed in this study enabled us to discover phases (Extended Data Fig. 6) that would be otherwise difficult to obtain through more conventional material synthesis routes.

Online content

Any methods, additional references, Nature Portfolio reporting summaries, source data, extended data, supplementary information, acknowledgements, peer review information; details of author contributions and competing interests; and statements of data and code availability are available at https://doi.org/10.1038/s41563-024-02023-7.

References

1. Armand, M. & Tarascon, J.-M. Building better batteries. *Nature* **451**, 652–657 (2008).
2. Tarascon, J. M. Is lithium the new gold? *Nat. Chem.* **2**, 510 (2010).
3. Yabuuchi, N. et al. Research development on sodium-ion batteries. *Chem. Rev.* **114**, 11636–11682 (2014).
4. Delmas, C. Sodium and sodium-ion batteries: 50 years of research. *Adv. Energy Mater.* **8**, 1703137 (2018).
5. Masquelier, C. & Croguennec, L. Polyanionic (phosphates, silicates, sulfates) frameworks as electrode materials for rechargeable Li (or Na) batteries. *Chem. Rev.* **113**, 6552–6591 (2013).
6. Han, M. H., Gonzalo, E., Singh, G. & Rojo, T. A comprehensive review of sodium layered oxides: powerful cathodes for Na-ion batteries. *Energy Environ. Sci.* **8**, 81–102 (2015).
7. Hosaka, T., Kubota, K., Hameed, A. S. & Komaba, S. Research development on K-ion batteries. *Chem. Rev.* **120**, 6358–6466 (2020).
8. Hasa, I. et al. Challenges of today for Na-based batteries of the future: from materials to cell metrics. *J. Power Sources* **482**, 228872 (2021).
9. Singh, B. et al. A chemical map of NaSICON electrode materials for sodium-ion batteries. *J. Mater. Chem. A* **9**, 281–292 (2021).
10. Ouyang, B. et al. Synthetic accessibility and stability rules of NASICONs. *Nat. Commun.* **12**, 5752 (2021).
11. Uebou, Y. et al. Electrochemical sodium insertion into the 3D-framework of $Na_3M_2(PO_4)_3$ (M=Fe, V). *Rep. Inst. Adv. Mater. Study Kyushu Univ.* **16**, 1–5 (2002).
12. Lim, S. Y., Kim, H., Shakoor, R. A., Jung, Y. & Choi, J. W. Electrochemical and thermal properties of NASICON structured $Na_3V_2(PO_4)_3$ as a sodium rechargeable battery cathode: a combined experimental and theoretical study. *J. Electrochem. Soc.* **159**, A1393–A1397 (2012).
13. Saravanan, K., Mason, C. W., Rudola, A., Wong, K. H. & Balaya, P. The first report on excellent cycling stability and superior rate capability of $Na_3V_2(PO_4)_3$ for sodium ion batteries. *Adv. Energy Mater.* **3**, 444–450 (2013).
14. Ishado, Y., Inoishi, A. & Okada, S. Exploring factors limiting three-Na^+ extraction from $Na_3V_2(PO_4)_3$. *Electrochemistry* **88**, 457–462 (2020).
15. Park, S. et al. Crystal structure of $Na_2V_2(PO_4)_3$, an intriguing phase spotted in the $Na_3V_2(PO_4)_3$-$Na_1V_2(PO_4)_3$ system. *Chem. Mater.* **34**, 451–462 (2022).
16. Wang, Z. et al. Phase stability and sodium-vacancy orderings in a NaSICON electrode. *J. Mater. Chem. A* **10**, 209–217 (2022).
17. Zakharkin, M. V. et al. Electrochemical properties and evolution of the phase transformation behavior in the NASICON-type $Na_{3+x}Mn_xV_{2-x}(PO_4)_3$ ($0 \le x \le 1$) cathodes for Na-ion batteries. *J. Power Sources* **470**, 228231 (2020).
18. Orikasa, Y. et al. Direct observation of a metastable crystal phase of Li_xFePO_4 under electrochemical phase transition. *J. Am. Chem. Soc.* **135**, 5497–5500 (2013).
19. Chotard, J.-N. et al. Discovery of a sodium-ordered form of $Na_3V_2(PO_4)_3$ below ambient temperature. *Chem. Mater.* **27**, 5982–5987 (2015).
20. Delacourt, C., Poizot, P., Tarascon, J. M. & Masquelier, C. The existence of a temperature-driven solid solution in Li_xFePO_4 for $0 \le x \le 1$. *Nat. Mater.* **4**, 254–260 (2005).
21. Lu, J., Oyama, G., Nishimura, S. I. & Yamada, A. Increased conductivity in the metastable intermediate in Li_xFePO_4 electrode. *Chem. Mater.* **28**, 1101–1106 (2016).
22. Delacourt, C., Rodríguez-Carvajal, J., Schmitt, B., Tarascon, J. M. & Masquelier, C. Crystal chemistry of the olivine-type Li_xFePO_4 system ($0 \le x \le 1$) between 25 and 370 °C. *Solid State Sci.* **7**, 1506–1516 (2005).
23. Chen, G., Song, X. & Richardson, T. J. Metastable solid-solution phases in the $LiFePO_4$/$FePO_4$ system. *J. Electrochem. Soc.* **154**, A627–A632 (2007).
24. Dodd, J. L., Yazami, R. & Fultz, B. Phase diagram of Li_xFePO_4. *Electrochem. Solid State Lett.* **9**, 151–155 (2006).
25. Nishimura, S. I., Natsui, R. & Yamada, A. Superstructure in the metastable intermediate-phase $Li_{2/3}FePO_4$ accelerating the lithium battery cathode reaction. *Angew. Chem. Int. Ed.* **54**, 8939–8942 (2015).
26. Delmas, C., Cherkaoui, F., Nadiri, A. & Hagenmuller, P. A NASICON-type phase as intercalation electrode: $NaTi_2(PO_4)_3$. *Mater. Res. Bull.* **22**, 631–639 (1987).
27. Delmas, C. & Nadiri, A. The chemical short circuit method. An improvement in the intercalation-deintercalation techniques. *Mater. Res. Bull.* **23**, 65–72 (1988).
28. Hagenmuller, P. & Delmas, C. Intercalation in 3-D skeleton structures: ionic and electronic features. *MRS Online Proc. Libr.* **210**, 323–334 (1990).
29. d'Yvoire, F., Pintard-Scrépel, M., Bretey, E. & de la Rochère, M. Phase transitions and ionic conduction in 3D skeleton phosphates $A_3M_2(PO_4)_3$: A = Li, Na, Ag, K; M = Cr, Fe. *Solid State Ion.* **9–10**, 851–857 (1983).
30. Patoux, S., Rousse, G., Leriche, J. B. & Masquelier, C. Structural and electrochemical studies of rhombohedral $Na_2TiM(PO_4)_3$ and $Li_{1.6}Na_{0.4}TiM(PO_4)_3$ (M = Fe, Cr) phosphates. *Chem. Mater.* **15**, 2084–2093 (2003).
31. Kawai, K., Asakura, D., Nishimura, S.-I. & Yamada, A. Stabilization of a 4.5 V Cr^{4+}/Cr^{3+} redox reaction in NASICON-type $Na_3Cr_2(PO_4)_3$ by Ti substitution. *Chem. Commun.* **55**, 13717–13720 (2019).
32. Wang, D. et al. Sodium vanadium titanium phosphate electrode for symmetric sodium-ion batteries with high power and long lifespan. *Nat. Commun.* **8**, 15888 (2017).
33. Lalere, F., Seznec, V., Courty, M., Chotard, J. N. & Masquelier, C. Coupled X-ray diffraction and electrochemical studies of the mixed Ti/V-containing NASICON: $Na_2TiV(PO4)_3$. *J. Mater. Chem. A* **6**, 6654–6659 (2018).
34. Wang, Z. et al. Kinetic Monte Carlo simulations of sodium ion transport in NaSICON electrodes. *ACS Mater. Lett.* **5**, 2499–2507 (2023).
35. Chen, F. et al. A NASICON-type positive electrode for Na batteries with high energy density: $Na_4MnV(PO_4)_3$. *Small Methods* **3**, 1800218 (2018).
36. Park, S. et al. An asymmetric sodium extraction/insertion mechanism for the Fe/V-mixed NASICON $Na_4FeV(PO_4)_3$. *Chem. Mater.* **34**, 4142–4152 (2022).
37. Lalère, F. et al. Improving the energy density of $Na_3V_2(PO_4)_3$-based positive electrodes through V/Al substitution. *J. Mater. Chem. A* **3**, 16198–16205 (2015).
38. Liu, R. et al. Exploring highly reversible 1.5-electron reactions ($V^{3+}/V^{4+}/V^{5+}$) in $Na_3VCr(PO_4)_3$ cathode for sodium-ion batteries. *ACS Appl. Mater. Interfaces* **9**, 43632–43639 (2017).
39. Ghosh, S., Jose, N., Senthilkumar, B., Amonpattaratkit, P. & Senguttuvan, P. Multi-redox ($V^{5+}/V^{4+}/V^{3+}/V^{2+}$) driven asymmetric sodium (de)intercalation reactions in NASICON-$Na_3VIn(PO_4)_3$ cathode. *J. Electrochem. Soc.* **168**, 050534 (2021).
40. Inoishi, A., Yoshioka, Y., Zhao, L., Kitajou, A. & Okada, S. Improvement in the energy density of $Na_3V_2(PO_4)_3$ by Mg substitution. *Chem ElectroChem* **4**, 2755–2759 (2017).
41. Zhou, W. et al. $Na_xMV(PO_4)_3$ (M = Mn, Fe, Ni) structure and properties for sodium extraction. *Nano Lett.* **16**, 7836–7841 (2016).
42. Zakharkin, M. V. et al. Enhancing Na^+ extraction limit through high voltage activation of the NASICON-type $Na_4MnV(PO_4)_3$ cathode. *ACS Appl. Energy Mater.* **1**, 5842–5846 (2018).
43. Xu, C. et al. Mn-rich phosphate cathodes for Na-ion batteries with superior rate performance. *ACS Energy Lett.* **7**, 97–107 (2022).

44. Soundharrajan, V. et al. The advent of manganese-substituted sodium vanadium phosphate-based cathodes for sodium-ion batteries and their current progress: a focused review. *J. Mater. Chem. A* **10**, 1022–1046 (2022).
45. Buryak, N. S. et al. High-voltage structural evolution and its kinetic consequences for the $Na_4MnV(PO_4)_3$ sodium-ion battery cathode material. *J. Power Sources* **518**, 230769 (2022).
46. Anishchenko, D. V., Zakharkin, M. V., Nikitina, V. A., Stevenson, K. J. & Antipov, E. V. Phase boundary propagation kinetics predominately limit the rate capability of NASICON-type $Na_{3+x}Mn_xV_{2-x}(PO_4)_3$ (0≤x≤1) materials. *Electrochim. Acta* **354**, 136761 (2020).
47. Ghosh, S. et al. High capacity and high-rate NASICON-$Na_{3.75}V_{1.25}Mn_{0.75}(PO_4)_3$ cathode for Na-ion batteries via modulating electronic and crystal structures. *Adv. Energy Mater.* **10**, 1902918 (2020).
48. Park, S. et al. Irreversible electrochemical reaction at high voltage induced by distortion of Mn and V structural environments in $Na_4MnV(PO_4)_3$. *Chem. Mater.* **35**, 3181–3195 (2023).
49. Perfilyeva, T. I. et al. Complete three-electron vanadium redox in NASICON-type $Na_3VSc(PO_4)_3$ electrode material for Na-ion batteries. *J. Electrochem. Soc.* **168**, 110550 (2021).
50. Park, S. et al. Crystal structures and local environments of NASICON-type $Na_3FeV(PO_4)_3$ and $Na_4FeV(PO_4)_3$ positive electrode materials for Na-ion batteries. *Chem. Mater.* **33**, 5355–5367 (2021).
51. Hadouchi, M. et al. Fast sodium intercalation in $Na_{3.41}£_{0.59}FeV(PO_4)_3$: a novel sodium-deficient NASICON cathode for sodium-ion batteries. *Energy Storage Mater.* **35**, 192–202 (2021).
52. de Boisse, B. M., Ming, J., Nishimura, S. & Yamada, A. Alkaline excess strategy to NASICON-type compounds towards higher-capacity battery electrodes. *J. Electrochem. Soc.* **163**, A1469–A1473 (2016).
53. Xu, C. et al. A novel NASICON-typed $Na_4VMn_{0.5}Fe_{0.5}(PO_4)_3$ cathode for high-performance Na-ion batteries. *Adv. Energy Mater.* **11**, 2100729 (2021).

[1]Laboratoire de Réactivité et de Chimie des Solides, Université de Picardie Jules Verne, CNRS, Amiens, France. [2]Institut de Chimie de la Matière Condensée de Bordeaux (ICMCB), Université de Bordeaux, Bordeaux INP, CNRS, Pessac, France. [3]TIAMAT, Amiens, France. [4]Department of Materials Science and Engineering, National University of Singapore, Singapore, Singapore. [5]Department of Materials Science and Engineering, Northwestern University, Evanston, IL, USA. [6]Réseau Français sur le Stockage Electrochimique de l'Energie (RS2E), CNRS, Amiens, France. [7]ALBA Synchrotron, Consortium for the Exploitation of the Synchrotron Light Laboratory (CELLS), Cerdanyola del Vallès, Spain. [8]Chemical and Biomolecular Engineering, National University of Singapore, Singapore, Singapore. [9]Department of Electrical and Computer Engineering, University of Houston, Houston, TX, USA. [10]Institut Universitaire de France, Paris, France. [11]These authors contributed equally: Sunkyu Park, Ziliang Wang. ✉e-mail: pcanepa@central.uh.edu; laurence.croguennec@icmcb.cnrs.fr; Christian.masquelier@u-picardie.fr

Methods

Synthesis of $Na_3V_2(PO_4)_3$

A carbon-coated VPO_4 precursor was first synthesized by mixing stoichiometric amounts of V_2O_5 (Alfa Aesar, 99.6%), H_3PO_4 (Alfa Aesar, 85%) and agar-agar (Fisher BioReagents) in deionized water to yield a solution that was stirred overnight in an oil bath at 80 °C. A solid residue was obtained, followed by further drying for 12 h overnight in the oven at 250 °C, before being ground again and heated at 890 °C for 2 h in an Ar atmosphere. After that, Na_3PO_4 (Acros Organics, 96%) was mixed with the resulting carbon-coated VPO_4 in a molar ratio of 1:2, and then heated at 800 °C for 2 h in an Ar atmosphere to obtain carbon-coated $Na_3V_2(PO_4)_3$. The prepared pristine $Na_3V_2(PO_4)_3$ powder contains agglomerates of several to tens of micrometres (Supplementary Fig. 2). The carbon content within the carbon-coated $Na_3V_2(PO_4)_3$ powder was about 1.8% in mass, as determined by thermogravimetric analysis (Supplementary Fig. 3).

Preparation of $Na_1V_2(PO_4)_3$ via chemical oxidation process

The $Na_3V_2(PO_4)_3$ powder was dispersed in acetonitrile (Sigma-Aldrich, 99.8%) using a magnetic stirrer, and a stoichiometric amount of a 0.1 M solution of nitronium tetrafluoroborate (Sigma-Aldrich, 95%) in acetonitrile was introduced dropwise into the first solution to produce the following chemical reaction:

$$Na_3V_2(PO_4)_3 + 2NO_2BF_4 \rightarrow Na_1V_2(PO_4)_3 + 2NaBF_4 + 2NO_2 \uparrow .$$

The resulting dispersed powder in the solution was then filtered and washed with acetonitrile. The whole process was performed in an Ar-filled glove box. The Na/V/P stoichiometry ratios obtained from inductively coupled plasma spectroscopy for $Na_3V_2(PO_4)_3$ and $Na_1V_2(PO_4)_3$ are 3.04(5)/1.97(1)/2.99(4) and 1.01(5)/1.99(2)/2.99(3), respectively, in very good agreement with the target compositions.

Synthesis of $Na_xV_2(PO_4)_3$

$Na_xV_2(PO_4)_3$ compositions (x = 1.5, 1.75, 2, 2.25, 2.5) can be prepared with the corresponding molar ratio of $Na_3V_2(PO_4)_3$ and $Na_1V_2(PO_4)_3$ powders followed by a heat treatment in Ar atmosphere according to the following chemical reaction:

$$y\,Na_3V_2(PO_4)_3 + (1-y)Na_1V_2(PO_4)_3 \rightarrow Na_{1+2y}V_2(PO_4)_3$$
$$(1+2y = x; 0.25 < y < 0.75).$$

Indeed, powders of these two end members ($yNa_3V_2(PO_4)_3 + (1-y)Na_1V_2(PO_4)_3$) were thoroughly mixed, pelletized and sealed in a gold tube in an Ar-filled glove box prior to annealing at 500–550 °C for 12 h. $Na_{1.5}V_2(PO_4)_3$ was obtained by chemical oxidation and deintercalation of 1.5 Na^+ ions from $Na_3V_2(PO_4)_3$ by adjusting precisely the concentration of NO_2BF_4 followed by a subsequent thermal treatment at 550 °C. Temperature-controlled in situ XRD patterns of mixtures of the precursors according to $yNa_3V_2(PO_4)_3 + (1-y)Na_1V_2(PO_4)_3$ ($0.25 \le y \le 0.75$) are given in Supplementary Fig. 1a–e, with y = 0.25, 0.375, 0.5, 0.625 and 0.75.

Chemical analysis

The carbon content within the carbon-coated $Na_3V_2(PO_4)_3$ powder was determined by thermogravimetric analysis combined with mass spectroscopy (using a NETZSCH STA 449 C) heated to 680 °C at a heating rate of 10 °C min^{-1} (Supplementary Fig. 3). The morphology of the powder was investigated by scanning electron microscopy with a Hitachi Model S-4500 microscope. The chemical compositions of the $Na_xV_2(PO_4)_3$ powders were controlled using inductively coupled plasma optical emission spectroscopy with a Varian model 720-ES spectrometer after the samples were dissolved in concentrated HCl solution under heating.

X-ray diffraction

Temperature-controlled in situ SXRD measurements were performed using a 0.5-mm-diameter capillary in transmission mode (Debye–Scherrer geometry), at a wavelength of 0.95289 Å at the MSPD beamline of the ALBA Synchrotron, Spain. The SXRD patterns were collected during heating/cooling ramps of 5 °C min^{-1}. On-the-fly data were collected for 20 s each so that a pattern was collected every ~3 °C. Every 50 °C, a longer acquisition of ~8 min was performed while keeping the temperature constant. The mixture of $Na_3V_2(PO_4)_3$ and $Na_1V_2(PO_4)_3$ in a molar ratio of 1:1 (that is, for $Na_xV_2(PO_4)_3$ with x = 2) was heated to 500 °C and then cooled to 35 °C. The formation of various $Na_xV_2(PO_4)_3$ compositions (x = 1.75, 2, 2.25 and 2.5) was also monitored by temperature-controlled XRD measurements with a laboratory bench X-ray Co $K\alpha_{1,2}$ radiation in reflection geometry (PANalytical X'Pert Pro). The XRD patterns were collected every 50 °C from 25 °C up to 500–550 °C (the sample being in a closed system filled with He gas), and then during cooling to 25 °C, with 1 h of acquisition for each pattern.

Electrochemical measurements

Electrochemical experiments were carried out with a half-cell configuration versus Na metal in a coin-cell set-up. Positive electrodes were made of the active material, carbon black (Alfa Aesar, 99.9+%) and polyvinylidene difluoride, with a weight ratio of 73:18:9 and with a mass loading of 6–8 mg cm^{-2}. One Celgard and one Whatman glass fibre (grade GF/D) sheets were used as separators, and the electrolyte was 1 M $NaPF_6$ in a mixture of ethylene-carbonate/dimethyl-carbonate (1:1, w/w) with 2 wt% of fluoroethylene carbonate. Battery cells were operated at a rate of C/10 (corresponding to the exchange of one Na^+ and one electron in 10 h) in the voltage window of 2.5–4.3 V versus Na^+/Na.

Operando X-ray diffraction

Operando XRD measurements were performed using an in situ cell (equipped with a beryllium window) placed in a PANalytical Empyrean diffractometer using Cu $K\alpha_{1,2}$ radiation in reflection mode. Each XRD pattern was collected with an acquisition time of 1 h in the 2θ angular range of 12–40°, with a 2θ step size of 0.0167°. The working electrodes were composed of the chemically prepared $Na_2V_2(PO_4)_3$ powder mixed with carbon black (80/20 in wt%), and Na metal was used as the counter electrode. Two different voltage regions were investigated, 2.5–4.4 V and 1.3–3.0 V versus Na^+/Na, at a rate of C/10 (one Na per formula unit within 10 h). The analysis of the XRD data was performed using the Rietveld method with FullProf Suite software. Note that operando measurements were done with a laboratory X-ray set-up in Bragg Brentano geometry (reflection), using an in situ cell with a Be window protected with an Al foil. Consequently, the intensities of the diffraction peaks at low 2θ angles are substantially affected by absorption (of Be and of the sample itself) but can be mathematically corrected based on the mass attenuation coefficient. The XRD patterns of $Na_2V_2(PO_4)_3$ collected from SXRD, from lab XRD with a standard holder, from lab XRD in an in situ cell and before and after the intensity correction are compared in Supplementary Fig. 4. The results of the Rietveld refinements are compared in Supplementary Table 1. A detailed procedure for the correction of the intensities is given in the Supplementary Information. Despite this correction, the intensity of the (012) reflection peak recorded at a low angle (Q = 0.017 $Å^{-1}$) in an in situ cell remains lower than expected, thus affecting the values of the occupancy factors determined for the Na(1) and Na(2) sites by Rietveld refinements.

Computational methodology

In our prior theoretical work[16,34], we developed a first-principles multiscale model, combining a cluster expansion formalism parameterized on DFT-computed Na-vacancy configurations with Monte Carlo simulations, to investigate phase behaviours and Na^+ transport of $Na_xV_2(PO_4)_3$ positive electrode material during Na (de)intercalation (Supplementary Fig. 5). With the accuracy of first-principles DFT calculations

in the strongly constrained and appropriately normed (SCAN) level of theory[54], we investigated the solubility of Na over a wide range of sodium compositions (that is, $1 \le x \le 4$). We considered a large number of Na-vacancy configurations (850 in total). A comprehensive temperature versus composition phase diagram of $Na_xV_2(PO_4)_3$ was derived. A close inspection of our DFT-computed structures at $Na_1V_2(PO_4)_3$, $Na_{1.5}V_2(PO_4)_3$ and $Na_2V_2(PO_4)_3$ results in ground state and metastable compositions, which are characterized by fully occupied Na(1) sites and partially occupied Na(1) sites, respectively. The corresponding key properties (that is, relative energies above the ground state, volume and Na(1) and Na(2) occupations) can be generated by DFT fully structural relaxations, as summarized in Table 1.

Data availability

Experimental data for Figs. 1–5 are available via Nextcloud at https://extra.u-picardie.fr/nextcloud/index.php/s/tSZagY99WdkDnzY. The results of the electronic structure calculations and other simulations reported in this work are freely available via Zenodo at https://zenodo.org/records/13357637 (ref. 55). Source data are provided with this paper.

References

54. Sun, J., Ruzsinszky, A. & Perdew, J. Strongly constrained and appropriately normed semilocal density functional. *Phys. Rev. Lett.* **115**, 036402 (2015).
55. Wang, Z. & Canepa, P. caneparesearxh/paper_NM23072487B_NVPsolidsolution: V1. *Zenodo* https://doi.org/10.5281/zenodo.13357637 (2024).

Acknowledgements

We acknowledge C. Denage and E. Lebraud from the Institut de Chimie de la Matière Condensée de Bordeaux (ICMCB) for their support to prepare chemical and XRD experiments, as well as ALBA (Barcelona, Spain) for SXRD experiments on the MSPD beamline (proposal number 2002421208). We are also grateful to the Agence Nationale de la Recherche (ANR) and TIAMAT for the funding (CIFRE grant) of S. Park's PhD thesis. We thank the European Union's Horizon 2020 research and innovation programme under Marie Skłodowska-Curie grant agreement no. 945357 for funding part of K. Choudhary's PhD thesis, and the Région Nouvelle-Aquitaine and the French National Research Agency (STORE-EX Labex Project ANR-10-LABX-76-01) for the partial financial support of this research. P.C. acknowledges funding from the National Research Foundation under NRF Fellowship NRFF12-2020-0012. P.C., Z.W., C.M. and J.-N.C. are grateful to the ANR-NRF for the funding of the NRF2019-NRF-ANR073 Na-MASTER project.

Author contributions

The initial project of this work was conceived by L.C., C.M., J.-N.C. and P.C. Most of the experimental work was performed by S.P. and K.C., supervised by J.-N.C., D.C., L.C., F.F. and C.M. Most of the computational work was performed by Z.W., supervised by P.C. The initial draft of the manuscript was written by S.P., and all the authors contributed heavily to the discussion and final version of this manuscript. All authors were consulted and gave their written approval on the present contribution statement.

Competing interests

The authors declare no competing interests.

Additional information

Extended data is available for this paper at https://doi.org/10.1038/s41563-024-02023-7.

Supplementary information The online version contains supplementary material available at https://doi.org/10.1038/s41563-024-02023-7.

Correspondence and requests for materials should be addressed to Pieremanuele Canepa, Laurence Croguennec or Christian Masquelier.

Peer review information *Nature Materials* thanks Shinichi Komaba and the other, anonymous, reviewer(s) for their contribution to the peer review of this work.

https://doi.org/10.1038/s41563-024-02023-7

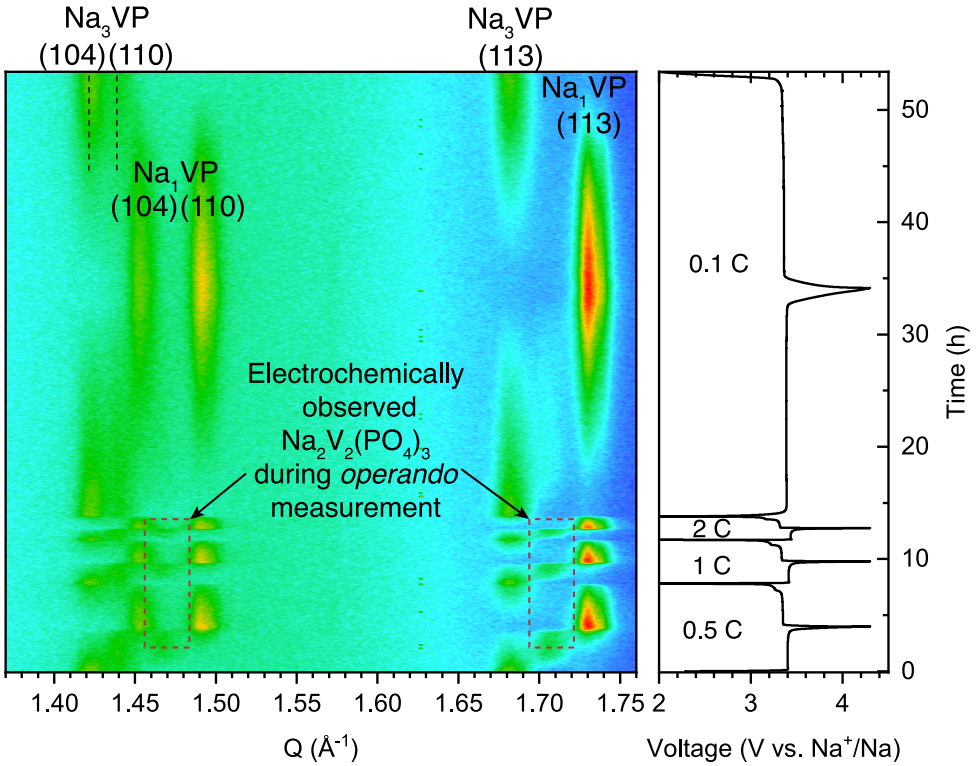

Extended Data Fig. 1 | Observation of the intermediate $Na_2V_2(PO_4)_3$ (Na_2VP) phase during battery operation. *Operando* XRD measurements using pristine $Na_3V_2(PO_4)_3$ as a positive electrode in a half cell versus Na metal. Voltage window of 2.0 – 4.3 V vs. Na^+/Na at cycling rates of C/10, C/2, 1 C and 2 C.

https://doi.org/10.1038/s41563-024-02023-7

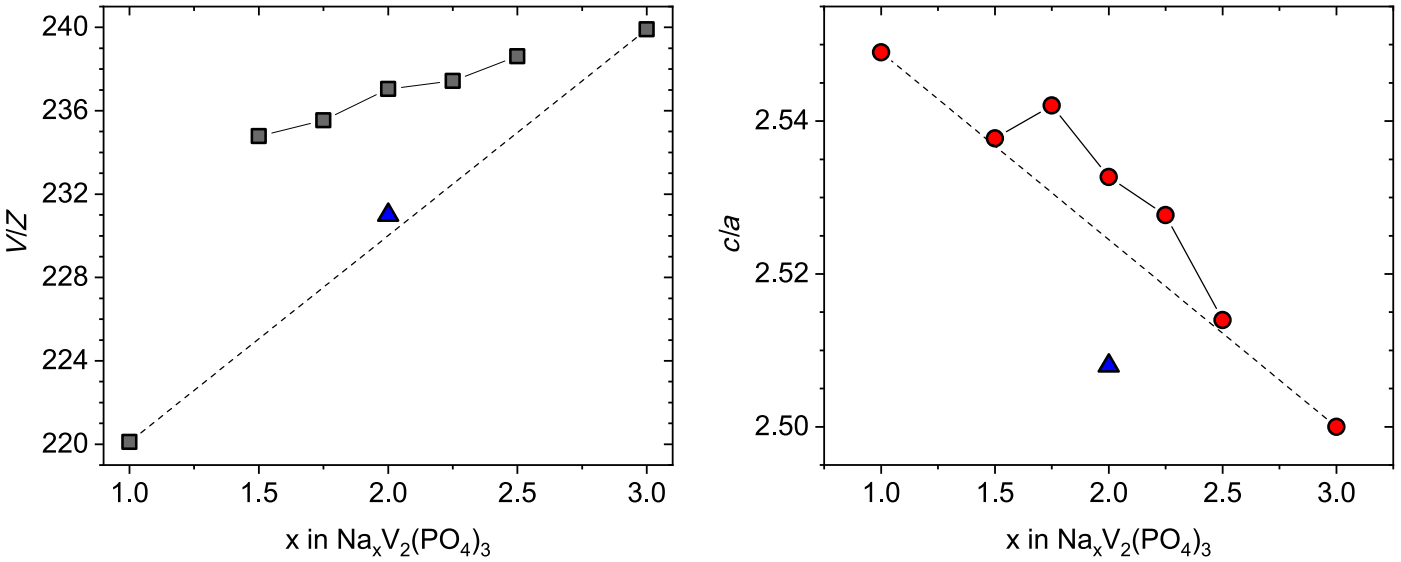

Extended Data Fig. 2 | Structural evolution of $Na_xV_2(PO_4)_3$. Unit cell volumes per formula unit (*V*/*Z*) and *c*/*a* ratios determined for chemically synthesized c-$Na_xV_2(PO_4)_3$ compositions at 25 °C, as a function of the Na_x content ($1 < x < 3$), and compared to those of $Na_3V_2(PO_4)_3$ and $Na_1V_2(PO_4)_3$. Note that the c-$Na_xV_2(PO_4)_3$ phases were prepared by annealing the mixtures of the two end-members, $Na_3V_2(PO_4)_3$ and $Na_1V_2(PO_4)_3$, with the appropriate molar ratios. The e-$Na_2V_2(PO_4)_3$ phase electrochemically observed during *operando* is marked with blue triangle. The standard deviation on each calculated value is smaller than the size of the symbol (black square or red circle). The dashed lines joining the end members' compositions are guides for the eye.

https://doi.org/10.1038/s41563-024-02023-7

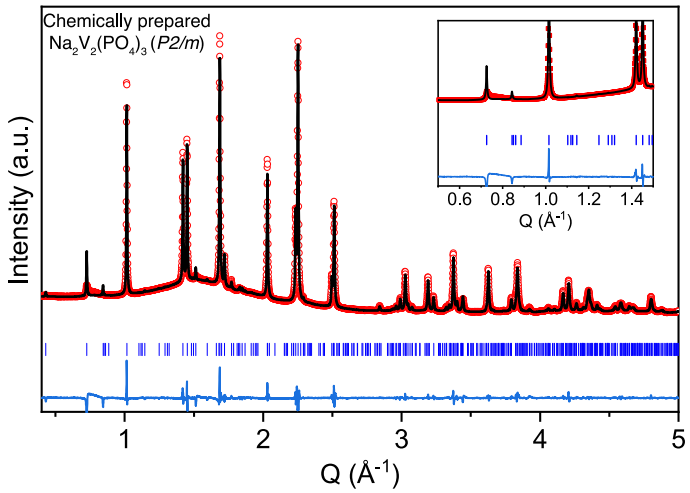

Extended Data Fig. 3 | Synchrotron XRD pattern of c-$Na_2V_2(PO_4)_3$. SXRD patterns of chemically prepared c-$Na_2V_2(PO_4)_3$ refined using a less symmetrical system (P2/m space group), indicating that the diffraction peaks at 0.65 - 0.9 in Q space are better explained.

https://doi.org/10.1038/s41563-024-02023-7

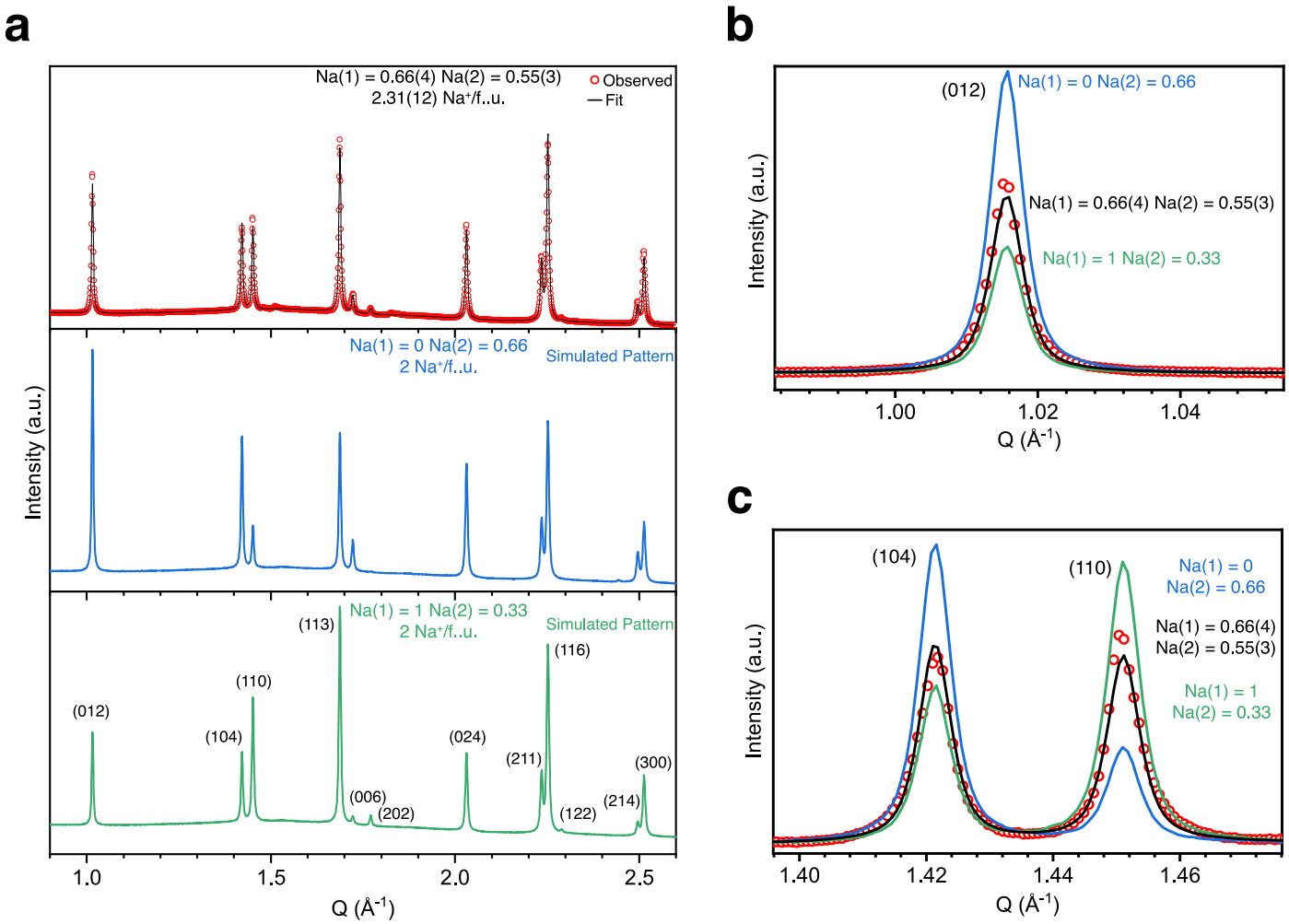

Extended Data Fig. 4 | Simulations of occupancy factors of Na(1) and Na(2) sites of c-$Na_2V_2(PO_4)_3$. (**a**) SXRD pattern of the chemically prepared c-$Na_2V_2(PO_4)_3$ with the refined results using R-3c space group, simulated SXRD patterns with Na(1) = 0, and Na(2) = 0.66 (blue), and Na(1) = 1, and Na(2) = 0.33 (green). Enlarged reflection peaks of (012) plane (**b**), and (104), (110) planes (**c**).

https://doi.org/10.1038/s41563-024-02023-7

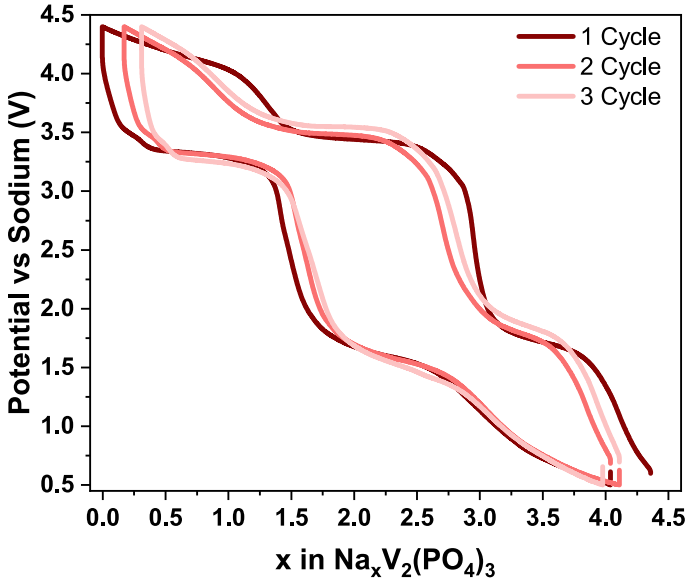

Extended Data Fig. 5 | The electrochemical cyclings of $Na_xV_2(PO_4)_3$ cathode. Global utilization of the $Na_xV_2(PO_4)_3$ framework with $0 \le x \le 4$, after the first discharge from OCV down to 0.5 V vs. Na^+/Na. Reminder, the first discharge voltage curve is omitted, and hence the first cycle started with charging process from $Na_4V_2(PO_4)_3$.

https://doi.org/10.1038/s41563-024-02023-7

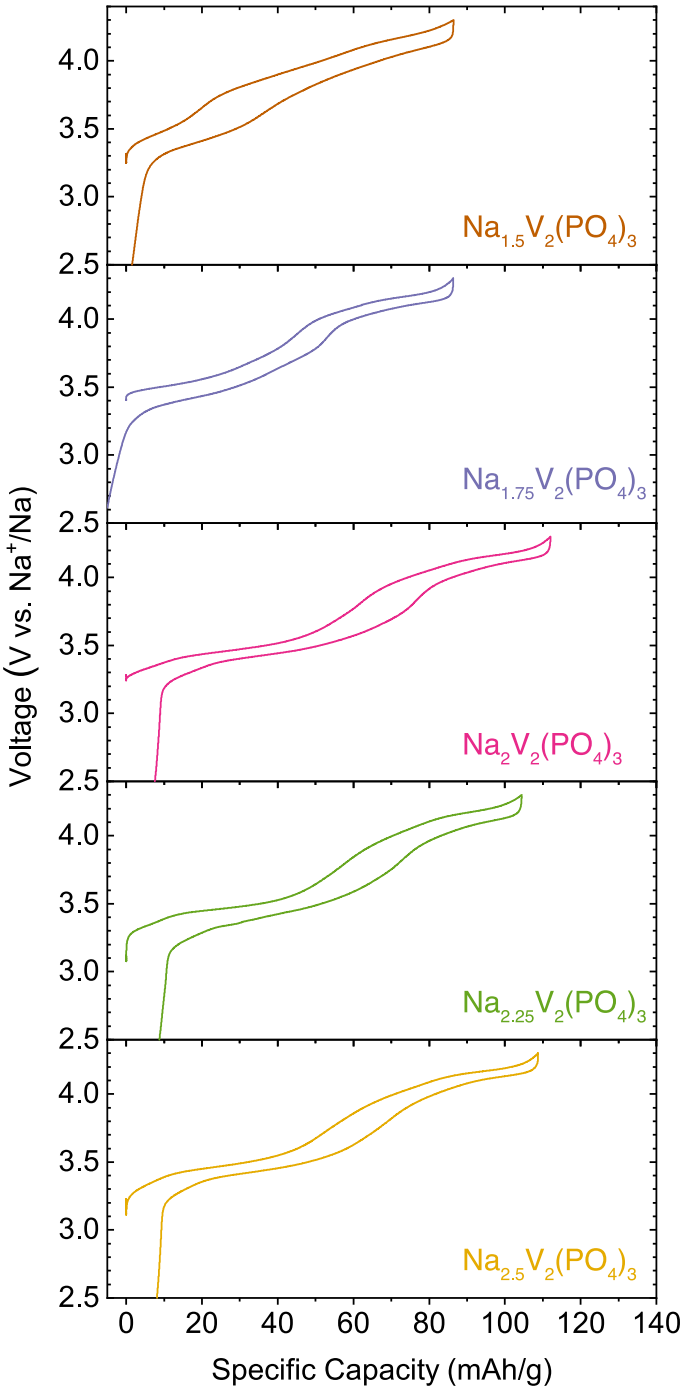

Extended Data Fig. 6 | Electrochemical (dis)charge profiles of the chemically synthesized $Na_xV_2(PO_4)_3$ cathodes. Electrochemical charge and discharge profiles of the chemically prepared c-$Na_xV_2(PO_4)_3$ (x = 1.5, 1.75, 2, 2.25, 2.5) electrode materials cycled between 2.5 and 4.3 V at C/10 (1 Na^+ in 10 h) versus Na metal.

https://doi.org/10.1038/s41563-024-02023-7

Extended Data Table 1 | Unit cell parameters, *V/Z* values, Na site occupancy factors, and average V-O distances determined from the Rietveld refinement of the electrochemically-observed $Na_2V_2(PO_4)_3$ and the chemically-prepared $Na_2V_2(PO_4)_3$. Note that the electrochemically-observed $Na_2V_2(PO_4)_3$ is described in both $P2_1/c$ and $R\text{-}3c$ space groups for comparison purposes. Note that the stoichiometry ratio obtained from ICP results for the chemically- prepared $Na_2V_2(PO_4)_3$ is $Na_{2.08(4)}V_{2.02(1)}(PO_4)_3$

	S.G.	a (Å)	b (Å)	c (Å)	c/a	β (°)	V/Z (Å^3)	Na(1) Occ.	Na(2) Occ.	Total Na /f.u.	V-O (Å)
Electrochemically-observed e-$Na_2V_2(PO_4)_3$	$P2_1/c$	15.2377(5)	8.6082(5)	8.7391(4)	–	126.281(3)	231.02(2)	0.98(4)	0.363(6)	2.1(3)	1.99(9) / 2.00(9)
	$R\text{-}3c$	8.6096(2)	8.6096(2)	21.5910(8)	2.508	120	231.003(13)	0.98(5)	0.33(2)	1.94(12)	1.98(2)
Chemically-prepared c-$Na_2V_2(PO_4)_3$	$R\text{-}3c$	8.6599(2)	8.6599(2)	21.8882(6)	2.528	120	236.929(13)	0.66(4)	0.55(3)	2.31(12)	2.001(7)

https://doi.org/10.1038/s41563-024-02023-7

Extended Data Table 2 | Unit cell parameters, *V*/*Z* values, Na site occupancy factors and average V-O distances determined from the Rietveld refinement of the XRD patterns collected *operando* during Na deintercalation from chemically-prepared c-$Na_2V_2(PO_4)_3$. Comparison with those obtained for chemically deintercalated $Na_2V_2(PO_4)_3$. *Refined and fixed at the last stages of refinement. Note that the stoichiometry ratio obtained from ICP results for the $Na_2V_2(PO_4)_3$ after the chemical de-sodiation process is $Na_{0.25(5)}V_{1.99(1)}(PO_4)_3$

	a (Å)	*c* (Å)	*c*/*a*	*V*/*Z* (Å^3)	Na(1) Occ.	Na(2) Occ.	Total Na /f.u.	V-O (Å)
Pristine	8.6497(4)	21.8865(14)	2.530	236.35(2)	0.70(6)	0.49(2)	2.18(12)	2.001(7)
Charged at 3.8 V	8.5383(3)	21.7706(16)	2.551	229.08(2)	0.85(4)	0.08(2)	1.09(9)	1.97(3)
Charged at 4.4 V	8.4732(3)	21.5117(15)	2.487	222.92(2)	0.46(4)	0.03(2)	0.55(11)	1.92(3)
Chemically deintercalated	8.4583(2)	21.6842(14)	2.507	223.92(12)	0.00(3)	0*	0.00(3)	1.89(15)
Discharged 3.9 V	8.5182(3)	21.7338(17)	2.551	227.62(2)	0.92(4)	0.04(3)	1.03(14)	1.97(3)
Discharged 2.5 V	8.6516(3)	21.8716(13)	2.528	236.29(2)	0.66(5)	0.54(2)	2.29(11)	2.03(3)

https://doi.org/10.1038/s41563-024-02023-7

Extended Data Table 3 | Refined structural parameters of chemically deintercalated phase from the $Na_2V_2(PO_4)_3$ powder collected within a capillary at 298 K. *Refined and fixed at the last stages of refinement

$Na_0V_2(PO_4)_3$
Space group: *R*-3*c* (#167); *Z* =6
a = 8.4583(2) Å; *c* = 21.6842(9) Å; *c*/*a* = 2.507
V = 1343.52(7) Å^3; *V*/*Z* = 223.920(12) Å^3
R_{wp} = 11.0 %; R_p = 14.6 %; R_{Bragg} = 5.11 %

Atom	Wyckoff position	*x*/*a*	*y*/*b*	*z*/*c*	Uiso, Å^2	Occ.
V(1)	12c	0	0	0.1451(3)	0.034(2)	1
P(1)	18e	0.2698(12)	0	0.25	0.091(5)	1
Na(1)	6b	0	0	0	0.074*	0.00(3)
Na(2)	18e	0.6420(13)	0	0.25	0.120*	0*
O(1)	36f	0.0241(16)	0.1929(15)	0.1911(6)	0.033(5)	1
O(2)	36f	0.1937(15)	0.1611(17)	0.0890(10)	0.120(6)	1